PHOTONICS Research

Experimental demonstration of high-Q MRR based on a germanium-on-insulator platform with an yttria insulator in the mid-IR range

Jinha Lim, Joonsup Shim, Inki Kim, and SangHyeon Kim*

School of Electrical Engineering, Korea Advanced Institute of Science and Technology (KAIST), Daejeon 34141, Republic of Korea
*Corresponding author: shkim.ee@kaist.ac.kr

Received 9 May 2023; revised 6 August 2023; accepted 28 August 2023; posted 28 August 2023 (Doc. ID 495076); published 1 November 2023

We experimentally demonstrate an all-pass microring resonator (MRR) based on a Y_2O_3 BOX germanium-on-insulator (GeOI) platform operating in the mid-IR region. The ring resonator was numerically designed to have a high quality (Q) factor in the 4.18 μm to 4.22 μm wavelength range in the fundamental TE mode. According to our design, the GeOI ring resonator was fabricated by the direct wafer-bonding technology with an yttria (Y_2O_3) buried oxide layer, which is transparent at the mid-IR region, for the bonding interface and the electron beam lithography. The experimental resonant characteristic was obtained using our fiber-based mid-IR measurement setup. The GeOI single MRR exhibited an extinction ratio (ER) of 15.28 dB and an insertion loss (IL) of 1.204 dB, and the racetrack showed an ER of 22.77 dB and an IL of 0.627 dB. Furthermore, the free spectral range of the device was 5.29 nm, and the loaded Q factor of 94,528 (176,158 of intrinsic Q factor) was extracted by the nonlinear least squares method. We believe this demonstration of our GeOI MRR offers a valuable opportunity to implement multipurpose devices such as optical sensors, switches, and filters in the mid-IR range.

https://doi.org/10.1364/PRJ.495076

1. INTRODUCTION

In photonic integrated circuits (PICs), a microring resonator (MRR) is an essential element to implement versatile functionalities with compactness such as optical switching, filtering, multiplexing, and modulation [1–4]. These functionalities can support numerous applications such as biosensing [5], spectroscopy [6], and electro-optical modulators [7]. Therefore, MRR optical switching and filtering are highly needed with a high extinction ratio (ER) and a quality (Q) factor. Also, the insertion loss (IL) of the ring resonator is an important parameter to realize the cascaded system in the PICs for on-chip integration. Recognizing these aspects, MRRs with a highly recorded Q factor ($\sim 10^8$) [8,9] and enhanced ER (55 dB) [10] in silicon photonics in the near-IR range have been emerging to achieve narrow bandwidth filtering and high modulation depth for high-resolution spectrometers and optical switching with a high on/off ratio. Despite the fact that a high-Q resonator is of great interest, a high ER resonator can be a powerful tool for an optical switch [11] with a high modulation depth to logically distinguish the signal on/off state and an optical sensor to detect the analyte with a high SNR for high sensitivity [12,13].

Meanwhile, the development of the PIC is extending to the mid-IR spectral range due to the promising potential opening new opportunities to explore unprecedented on-chip applications such as biochemical sensing, medical diagnosis, industrial processes, and thermal imaging [14–17]. These technologies are conceivable because of the superior molecular fingerprint in mid-IR spectroscopy by exploiting a tunable diode laser absorption spectroscopy [18]. Mid-IR spectroscopy measures optical absorption in the mid-IR range to analyze distinctive rovibrational dynamics in the intermolecular band of the analyte. In this regard, significant effort is presently being made to fabricate the mid-IR resonators for refractive index sensing to detect the analyte [19] or demultiplex the mid-IR wavelength to reach the next photonic elements [20]. Here, arrayed waveguide gratings (AWGs) [21] and tunable filters [22] have been generally proposed for the on-chip integrated demultiplexing spectrometer. In particular, filters such as microring and disk structures show an advantage in terms of tailoring the spectral response with high resolution and bandwidth by finely designing these photonic circuits. Although it is inevitable that the Q factor in the mid-IR band will be lower compared to the near-IR band due to the Q being inversely proportional to the wavelength, there is a distinct advantage: a reduced scattering loss caused by sidewall roughness. In addition, thanks to the wavelength scaling effect, the size of mid-IR devices is larger compared to the devices operating near-IR region. As a result, the fabrication process to accurately set the optical filtering

wavelength range becomes more manageable. This offers an additional advantage in the implementation of mid-IR devices.

Germanium (Ge) has been widely used in many mid-IR applications because of Ge's broadband transparency (up to 15 μm) and high refractive index ($n_{Ge} \sim 4$) for good optical confinement in the mid-IR region. Similar to silicon (Si) as a group IV semiconductor, Ge provides high-volume manufacturing and high compatibility with CMOS technology. In addition, Ge has a strong nonlinear effect among the mid-IR photonic platforms due to the Kerr nonlinear index n_2 of the Ge at the 4.2 μm wavelength being 25.5 nm^2/W [23]; on the other hand, the n_2 of Si is 3.29 nm^2/W. Thus, mid-IR photonic platforms based on Ge that can efficiently provide these advantages have been studied to further achieve a low optical loss [24–27]. In this regard, a Ge-based high Q ($\sim 10^5$) microresonator [28] was reported. Recently, a Ge-on-insulator (GeOI) with yttria (Y_2O_3; $n_{Y_2O_3} \sim 1.85$) as a buried oxide (BOX) layer was demonstrated in our previous work [29]. The Y_2O_3 is optically transparent in the broadband of the mid-IR range [30], as well as excellent interfacial material for wafer bonding of homogeneous/heterogeneous integration [31]. Accordingly, GeOI could be the promising platform for the implementation of mid-IR PICs.

In this work, we experimentally demonstrate what we believe, to the best of our knowledge, is the first all-pass MRR based on GeOI with the Y_2O_3 BOX at the mid-IR wavelength (λ). For the high ER and Q of the MRR, we designed the resonator with the narrow width of the bus waveguide to guide a strong evanescent field outer cladding region. The Y_2O_3-based GeOI wafer was manufactured by direct wafer-bonding (DWB) technology, electron-beam (EB) lithography, and ICP-based etching. Then, we measured the resonant characteristic of the GeOI MRR with our mid-IR optical fiber setup with an external cavity quantum cascade laser (EC-QCL) operating around λ of 4.2 μm. Furthermore, we analyzed the resonant characteristics of the GeOI MRR, including a racetrack-type MRR with the ER, IL, and free spectral range (FSR). Finally, the loaded Q factor (Q_L) of the GeOI MRR was extracted by high-resolution measurement followed by Lorentzian curve fitting with a nonlinear least square (NLSQ) method, and a benchmark of the Q_L for the mid-IR photonic platforms is delivered.

Figure 1(a) illustrates the schematic of the GeOI MRR with grating couplers, which were designed for around 4.2 μm λ in the TE polarization, and the indium fluoride (InF_3) single-mode fibers. The MRR was implemented on our GeOI wafer, which was obtained by the DWB with the 3 μm thick Y_2O_3 as a bonding interface as well as low-loss material in the broad mid-IR range [30,31]. The thickness of the Ge (H) was 500 nm, and the ring radius (R) was 63.5 μm to satisfy the resonant wavelength being 4.2 μm with an effective refractive index (n_{eff}) [Fig. 1(c)]. The width of the bus waveguide (W_{bus}), the width of the ring waveguide (W_{ring}), and the bus-to-ring gap (G) of the MRR were optimized by the optical simulation, which is shown in Fig. 1(b). For the high ER, which needs the strong light coupling between the bus and ring waveguide, the W_{bus} and W_{ring} were designed to be 1.2 μm considering the high evanescent field, where the confinement factor in the external region was 9.08% [30]. At λ of 4.2 μm, n_{eff} of 2.76 for the 1.2 μm width GeOI waveguide was obtained by the finite difference eigenmode solver (Ansys Lumerical), as shown in Fig. 1(c). Inevitable resonance splitting caused by the backscattering could occur due to the sidewall roughness [32] of the

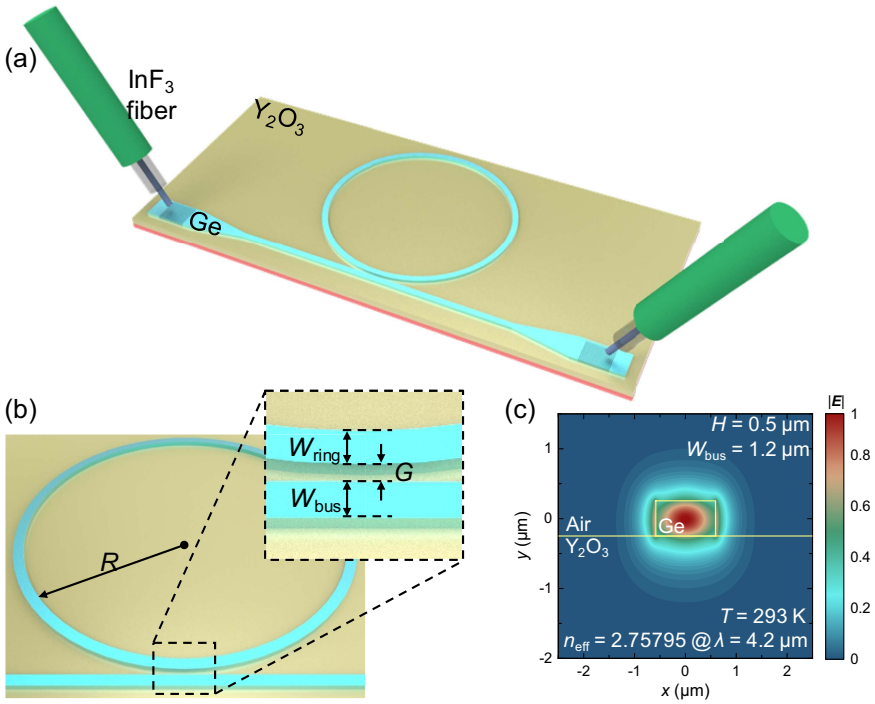

Fig. 1. (a) Schematic of the GeOI MRR for mid-IR range. (b) Magnified images of the ring part. (c) Electric field distribution and n_{eff} of the bus waveguide when W_{bus} was 1.2 μm.

waveguide. However, the roughness-induced dependency of the backscattering in the mid-IR range is relatively weaker than the near-IR band. Thus, the small sidewall roughness of our GeOI waveguides might not affect the resonance splitting at around the 4.2 μm band.

2. DESIGN AND FABRICATION

We predicted the resonant characteristic of the GeOI MRR by using a 3D finite-difference time-domain (3D FDTD) simulation (Ansys Lumerical). The material loss of the Ge caused by the free-carrier absorption effect was considered in the simulation owing to the phosphorus-doped n-type Ge (4×10^{-16} cm^{-3}) [29]. Figure 2(a) shows the transmission in the log scale at the output port of the GeOI MRR with R, W_{ring}, and W_{bus} of 63.5 μm, 1.2 μm, and 1.2 μm, respectively, for various gap G. For G values smaller than 0.5 μm, the resonator is overcoupled. Conversely, an undercoupling behavior was observed for G values exceeding 0.5 μm. Here, the highest ER of 16.2 dB corresponding to 162,513 of the Q factor in this simulation was exhibited when G of the GeOI MRR was 0.5 μm, which is the condition of the critical coupling in our case, as shown in Fig. 2(b). Figure 2(c) shows the magnitude of the electric field $|E|$ distribution of the GeOI MRR with an R of 63.5 μm, where G is 0.5 μm at 4.2 μm λ. The TE mode in the bus waveguide is well coupled to the ring waveguide and the resonance occurs within the ring, leading to a strong field distribution confined to the ring structure.

From the optical design, we fabricated our GeOI MRR for a high Q factor. To manufacture the GeOI wafer, as we described in detail in Ref. [29], a chemically cleaned Si (100) substrate and Ge epitaxial wafer grown on a Si substrate in the order of Ge strained relaxed buffer (SRB) (900 nm), $Si_{0.5}Ge_{0.5}$ (10 nm), and Ge (500 nm), were prepared. After the removal of native oxide on the surface, the 1.5 μm thick Y_2O_3 was deposited on both substrates using an RF sputter. Then the surface of the thick Y_2O_3 layer as a bonding interface on these substrates was chemically polished to achieve submicron surface roughness by the CMP machine with silica colloidal slurry. DWB with the Si and Ge epitaxial wafers was carried out while heating and pressing for a long time in the vacuum after the surface cleaning procedure and O_2 plasma treatment for both substrates. To selectively remove the unnecessary layers at the side of the Ge epitaxial wafer, these three steps were taken. First, mechanical grinding made the thick Si substrate thin, then

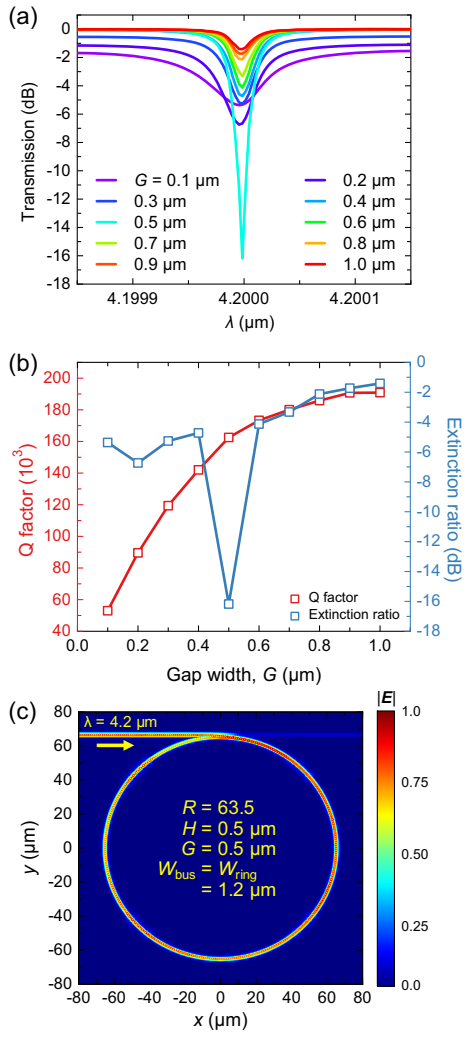

Fig. 2. (a) 3D FDTD simulation for the transmission of the GeOI MRR by varying the G at $\lambda = 4.2$ μm. (b) Extracted Q factor and ER for the result of (a). (c) Electric field distribution of the GeOI MRR with the indicated dimension in the graph at $\lambda = 4.2$ μm.

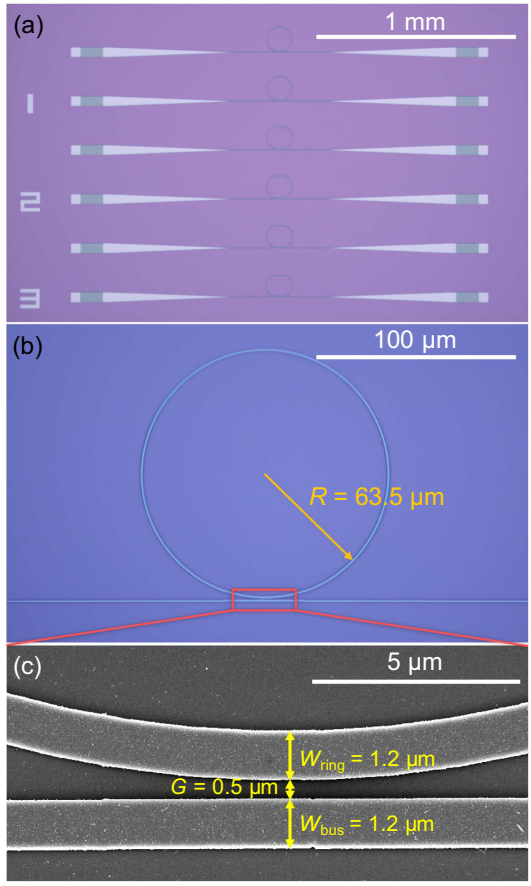

Fig. 3. (a) OM image of the GeOI MRR. (b) SEM image of the GeOI MRR with R of 50 μm. (c) Magnified image of the gap between the bus and ring waveguides.

the thinned Si and $Si_{0.5}Ge_{0.5}$ were chemically etched with tetramethyl ammonium hydroxide (TMAH) with diluted deionized water, and finally the Ge SRB was removed with an ammonia–peroxide mixture. This procedure describes the Y_2O_3-insulator-based GeOI for the mid-IR photonic platform. In the MRR manufacturing step, the GeOI was patterned by the EB lithography with negative EB resist followed by an inductively coupled plasma reactive ion etch in C_4F_8 and SF_6 environment. Finally, the EB resist was removed by the acetone and plasma treatment. Figure 3(a) shows the optical microscope image of the fabricated GeOI MRR, including the grating couplers (coupling efficiency; 9.9 dB at 4.2 μm λ) that were the same dimension in the previously reported GeOI devices [29]. The polarization of the mode relied on this grating coupler to couple 4.2 μm λ in the TE mode. The radius of the ring R was 63.5 μm, as shown in Fig. 3(b). According to the optimized EB lithography process, W_{bus}, W_{ring}, and G were successfully fabricated to satisfy the conditions of our optical design with 1.2 μm, 1.2 μm, and 0.5 μm, respectively, as shown in Fig. 3(c).

3. RESULT AND DISCUSSION

We characterized the GeOI MRR using our mid-IR optical fiber-based waveguide measurement setup. The setup was composed of the EC-QCL (MIRcat-QT, Daylight Solutions), an MCT detector (PVI-4TE-5, VIGO Photonics), and an InF_3-based optical fiber (Thorlabs). To avoid mid-IR optical absorption of carbon dioxide around $\lambda = 4.2$ μm, the part of the linear stages for the sample and fibers was encapsulated

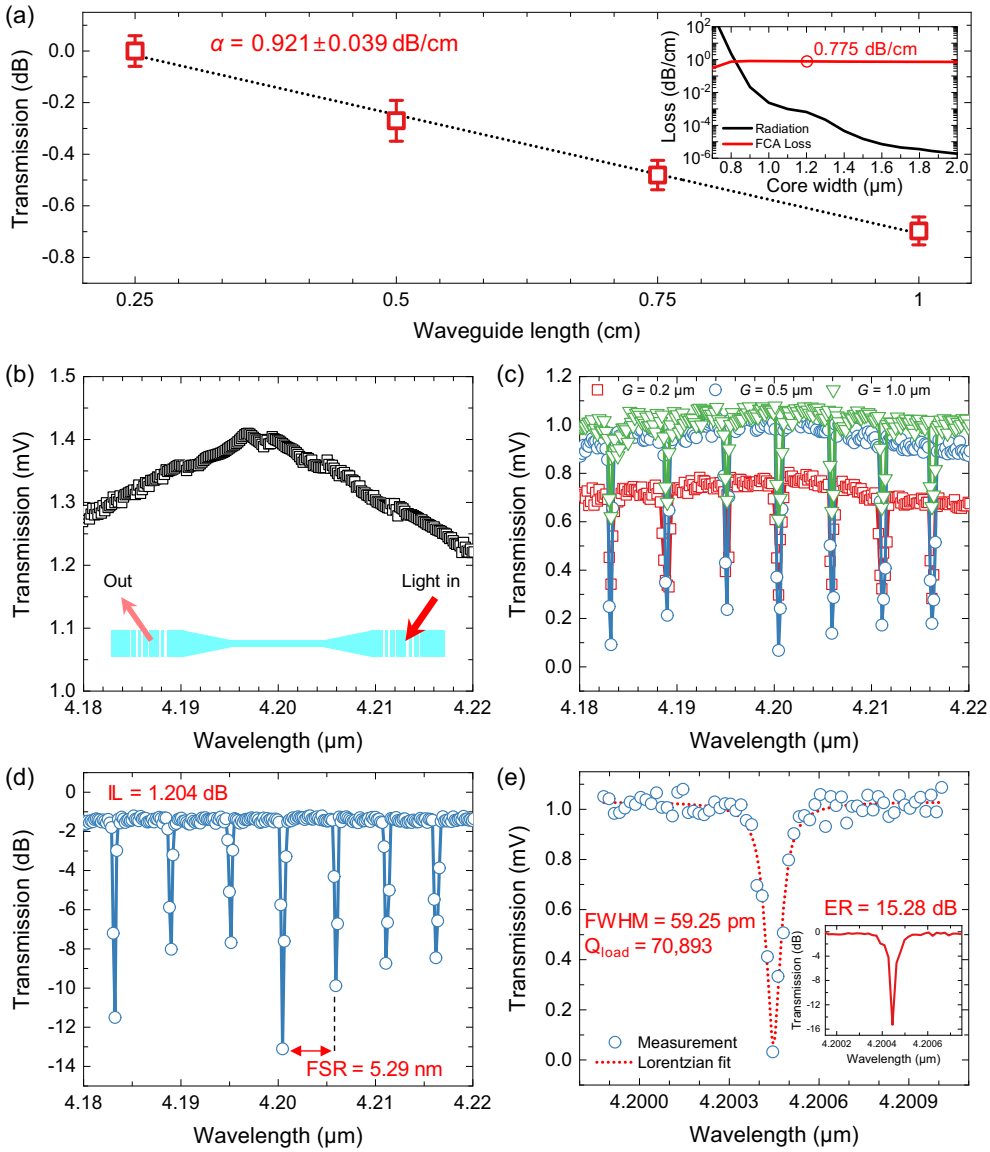

Fig. 4. (a) Propagation loss measurement of the GeOI waveguides at 4.2 μm λ using the cutback method. (b) Transmission spectrum of the GeOI straight-line waveguide. Inset: simulation of propagation loss with radiation and FCA loss for the GeOI waveguide at a 4.2 μm wavelength. (c) Transmission spectra of the GeOI MRRs with 0.2 μm, 0.5 μm, and 1.0 μm G at 4.18 μm to 4.22 μm λ with 63.5 μm of R for evaluation of the resonant characteristic. (d) Normalized transmission of the MRR ($G = 0.5$ μm) by the transmission of the straight-line waveguide in (b). (e) At 4.2 μm λ, the measurement for high-resolution resonance to estimate the Q_L of the MRR with an R of 63.5 μm.

by an acrylic chamber for N_2 gas injection by fully purging the gas inside the chamber. The mid-IR light from the EC-QCL is coupled to the input fiber by focusing the light with the mid-IR aspheric lens. Then, the mid-IR beam is coupled to the GeOI input grating coupler after the light-coupling out of the cleaved fiber facet. In our experimental setup, the optical power at the input fiber measured 70 mW after passing through various optical components and fibers. Considering the coupling efficiency of the grating coupler, thereafter, the coupled power through the GeOI MRR was approximately 7 mW, which is considered relatively low to induce significant nonlinear effects. Eventually, the mid-IR light propagating through the GeOI MRR is coupled out from the output grating coupler and recouples to the output fiber.

First, we measured the propagation loss (α) of the 1.2-μm-width GeOI waveguides by using the cutback method, as shown in Fig. 4(a). α was measured as 0.92 dB/cm. The dominant loss factor among the representative factors [radiation, free-carrier absorption (FCA), scattering, and BOX loss] [29] is the free-carrier absorption (0.775 dB/cm) in our GeOI waveguide, as shown in the inset of Fig. 4(a). It is attributed to the n-type doping of our Ge with a concentration of 4×10^{16} cm^{-3}. Therefore, a narrow width condition (1.2 μm of the Ge width) to effectively manage the impact of FCA loss was adopted, while simultaneously enhancing the external evanescent field through strong light coupling. Although further reduction of the waveguide width could potentially decrease FCA loss, it would also result in an abrupt increase in radiative loss,

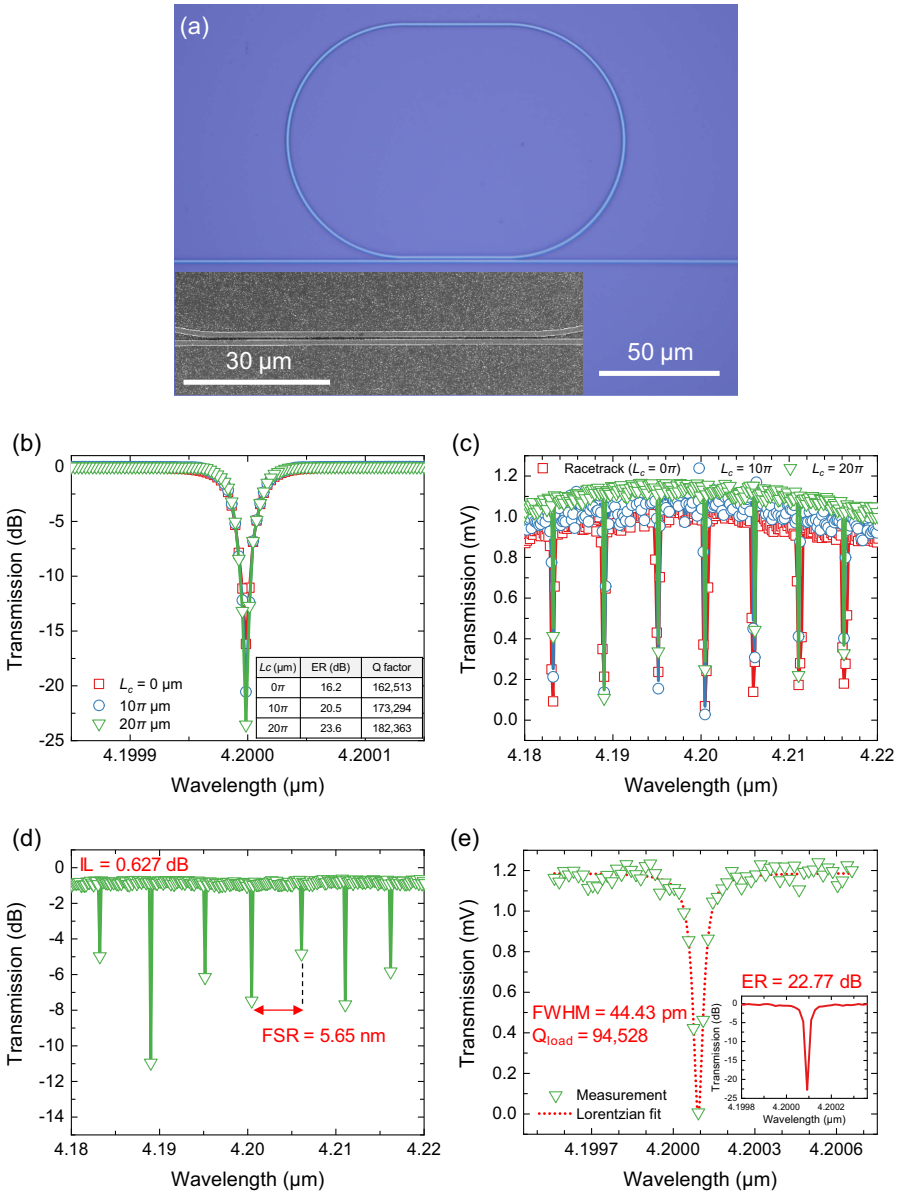

Fig. 5. (a) OM image of the racetrack MRR. Inset: magnified image of the coupling region. (b) 3D FDTD simulation for the transmission of the GeOI racetrack MRRs by varying the L_c at $\lambda = 4.2$ μm. (c) Transmission spectra for the racetrack MRRs at 4.18 μm to 4.22 μm λ. (d) Normalized transmission of the racetrack MRR ($L_c = 20$ μm) by the transmission of the straight-line waveguide. (e) Characterization of Q_L for the racetrack-type GeOI MRR at 4.2 μm λ.

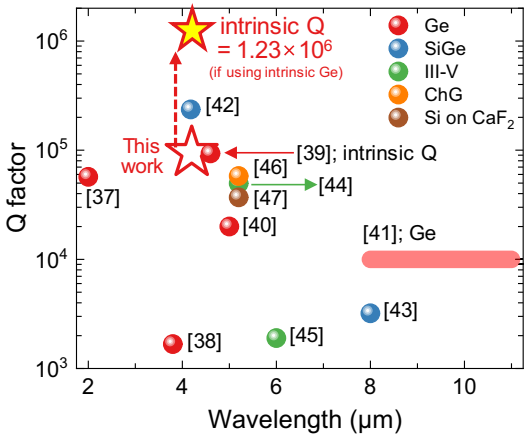

Fig. 6. Q_L benchmark for the available mid-IR platform-based MRRs.

leading to a degradation in the Q performance despite achieving stronger light coupling. Over the 0.9 μm width of the Ge, the influence of FCA loss reached saturation, and no additional loss reduction was possible. However, beyond this point, the intensity of light coupling gradually decreased, raising concerns about the potential deterioration in the resonator's performance. In Fig. 4(c), using our experimental setup we measured the transmission of the GeOI MRRs with three sizes of G with different coupling conditions: over coupling, critical coupling, and undercoupling resonances with 0.2, 0.5, and 1.0 μm, respectively, in the mid-IR band. The depth of the intensity trough is less significant in both the undercoupling and overcoupling conditions, compared to the critical coupling point. To extract IL, the obtained resonance curves were normalized by the straight-line waveguide, as shown in Fig. 4(b). When G was 0.5 μm, the IL and FSR were 1.204 dB and 5.29 nm, respectively. Additionally, the high-resolution measurement to evaluate the Q_L in the MRR was conducted at $\lambda = 4.2$ μm, as shown in Fig. 4(e). The dots in the graph are the measurement points for the resonant curve and the dash lines are Lorentzian fitting curves using the NLSQ method. As a result, the FWHM was 592.5 pm, corresponding to the loaded Q factor being 70,893 at $\lambda = 4.2$ μm. Here, the intrinsic Q factor (Q_I) was 120,973, which was obtained by using the expression in [33]. The high Q factor of the GeOI MRR is attributed to its very low propagation loss of 0.92 dB/cm.

Furthermore, we fabricated a racetrack-shaped MRR, as shown in Fig. 5(a), to enhance the coupling strength in the GeOI MRRs and carried out the measurements for the resonance curves of two coupling lengths (L_c) of 10π μm and 20π μm, as shown in Fig. 5(c). It is well known that racetrack resonators are one of the structures that can be used to achieve high Q factors. The improvement of the ER and Q factor was validated through 3D FDTD simulations of the transmission in the GeOI racetrack MRRs, as shown in Fig. 5(b), where both the ER and Q factor increased as L_c was extended. Here, the optical path of the racetrack resonator was maintained at the same length as the single MRR, when the coupling length was varied. Additionally, the racetrack resonator could be adopted to minimize bending losses, thereby contributing to higher Q factors compared to a single-ring resonator. Due to the long coupling length of the resonators, the ILs of the two racetrack resonators ($L_c = 10\pi$ μm and 20π μm) showed lower than the single MRR ($L_c = 0\pi$). As shown in Fig. 5(c), the IL and FSR were 0.627 dB and 5.65 nm, respectively. Although it is difficult to obtain an extremely high resolution due to the Q value being inversely proportional to the operating λ, a high Q_L of 94,528 (around $\sim 10^5$; $Q_I = 176{,}158$) in the 20π μm L_c GeOI racetrack resonator was achieved, as depicted in Fig. 5(c). From the result of this Q factor, we can derive theoretical absorption α with 1.017 dB/cm by using the relation $Q_I = 2\pi n_{\text{eff}}/(\lambda\alpha)$. With only a minor discrepancy of approximately 0.09 dB/cm observed between the loss extracted using the cutback method and the theoretically calculated loss derived from the measured Q factor, it can be concluded that our GeOI MRR is a well-designed and well-fabricated device. Indeed, the Q factor of the GeOI MRR could achieve an even higher value by modification of the ring structure (Euler bend [34], pulley-type coupler [35], and cascaded ring structure [36]). Moreover, using intrinsic Ge instead of the n-type doped Ge can lead to improved Q factors by suppressing propagation loss caused by the FCA effect. With intrinsic Ge, unwanted absorption from free carriers is minimized, resulting in higher Q factors in the waveguide and enhanced performance in photonic devices and applications.

Finally, we compared the Q_L of our result with several ring resonators in mid-IR platforms (Fig. 6) such as Ge [37–41], SiGe [42,43], InGaAs [44], GaAs [45], chalcogenide (ChG) [46], and Si on CaF_2 [47]. Among these platforms, the SiGe platform [42] exhibits the highest Q factor, with 236,000 at a 4.18 μm wavelength. Nonetheless, our result shows that our mid-IR ring resonator achieved the highest Q_L factor (94,528) value compared to the Ge-based platforms, demonstrating the effectiveness of our design approach to achieve high-performance IR photonic devices. Furthermore, considering the reduction of the FCA loss to 0.775 dB/cm through the fabrication of intrinsic Ge, the propagation loss of the GeOI waveguide could be decreased to 0.146 dB/cm. This would ideally result in an intrinsic Q factor of 1.23×10^6 at a 4.2 μm wavelength.

4. CONCLUSION

In conclusion, we presented what we believe, to the best of our knowledge, is the first experimental demonstration of low-loss, high-Q GeOI MRRs fabricated using the DWB of a Y_2O_3 lower cladding layer. By investigating the G dependency of the MRRs for critical coupling, the dimension of the GeOI MRR was determined with the narrow W (1.2 μm) and G (0.5 μm) for the strong evanescent coupling. The MRRs with the grating couplers, which operate at $\lambda = 4.2$ μm in the fundamental TE mode, were fabricated by EB lithography on our GeOI wafer. At the mid-IR spectra (4.18–4.22 μm), our GeOI MRR exhibited a high ER and low IL of 22.77 dB and 0.627 dB, respectively, and a Q_L of 94,528 where Q_I was 176,158 obtained at $\lambda = 4.2$ μm. We believe that the MRR, which has a high Q factor, could be realized by introducing advanced structures to the MRR. Hence, we believe this

is a major step toward the mid-IR PIC based on the new GeOI using Y_2O_3.

Funding. National Research Foundation of Korea (2023R1A2C2002777); KIST Institutional Program (Atmospheric Environment Research Program) (2E32302); BK FOUR.

Disclosures. The authors declare no conflicts of interest.

Data Availability. Data underlying the results presented in this paper are not publicly available at this time but may be obtained from the authors upon reasonable request.

REFERENCES

1. S. Ohno, Q. Li, N. Sekine, H. Tang, S. Monfray, F. Boeuf, K. Toprasertpong, S. Takagi, and M. Takenaka, "Si microring resonator optical switch based on optical phase shifter with ultrathin-InP/Si hybrid metal-oxide-semiconductor capacitor," Opt. Express **29**, 18502–18511 (2021).
2. P. Dong, W. Qian, H. Liang, R. Shafiiha, N.-N. Feng, D. Feng, X. Zheng, A. V. Krishnamoorthy, and M. Asghari, "Low Power and compact reconfigurable multiplexing devices based on silicon microring resonators," Opt. Express **18**, 9852–9858 (2010).
3. W. D. Sacher and J. K. Poon, "Dynamics of microring resonator modulators," Opt. Express **16**, 15741–15753 (2008).
4. Y. Yuan, W. V. Sorin, Z. Huang, X. Zeng, D. Liang, A. Kumar, S. Palermo, M. Fiorentino, and R. G. Beausoleil, "A 100 GB/s PAM4 two-segment silicon microring resonator modulator using a standard foundry process," ACS Photon. **9**, 1165–1171 (2022).
5. K. De Vos, I. Bartolozzi, E. Schacht, P. Bienstman, and R. Baets, "Silicon-on-insulator microring resonator for sensitive and label-free biosensing," Opt. Express **15**, 7610–7615 (2007).
6. S. N. Zheng, J. Zou, H. Cai, J. F. Song, L. K. Chin, P. Y. Liu, Z. P. Lin, D. L. Kwong, and A. Q. Liu, "Microring resonator-assisted Fourier transform spectrometer with enhanced resolution and large bandwidth in single chip solution," Nat. Commun. **10**, 2349 (2019).
7. M. Bahadori, Y. Yang, A. E. Hassanien, L. L. Goddard, and S. Gong, "Ultra-efficient and fully isotropic monolithic microring modulators in a thin-film lithium niobate photonics platform," Opt. Express **28**, 29644–29661 (2020).
8. K. Y. Yang, D. Y. Oh, S. H. Lee, Q.-F. Yang, X. Yi, B. Shen, H. Wang, and K. Vahala, "Bridging ultrahigh-*Q* devices and photonic circuits," Nat. Photonics **12**, 297–302 (2018).
9. M. W. Puckett, K. Liu, N. Chauhan, Q. Zhao, N. Jin, H. Cheng, J. Wu, R. O. Behunin, P. T. Rakich, K. D. Nelson, and D. J. Blumenthal, "422 million intrinsic quality factor planar integrated all-waveguide resonator with sub-MHz linewidth," Nat. Commun. **12**, 934 (2021).
10. J. Liu, J. Du, W. Shen, G. Zhou, L. Zhou, W. Zhang, K. Xu, and Z. He, "Ultrahigh extinction ratio silicon micro-ring modulator by MDM resonance for high speed PAM-4 and PAM-8 signaling," Opt. Express **30**, 25672–25684 (2022).
11. L. Zhou, L. Lu, S. Zhao, D. Li, Z. Guo, and J. Chen, "Silicon active microring resonators for optical switching," in *2016 Progress in Electromagnetic Research Symposium (PIERS)* (2016), p. 2621.
12. H. Zhu, I. M. White, J. D. Suter, P. S. Dale, and X. Fan, "Analysis of biomolecule detection with optofluidic ring resonator sensors," Opt. Express **15**, 9139–9146 (2007).
13. X. Ou, Y. Yang, F. Sun, P. Zhang, B. Tang, B. Li, R. Liu, D. Liu, and Z. Li, "Wide-range, ultra-compact, and high-sensitivity ring resonator biochemical sensor with CMOS-compatible hybrid plasmonic waveguide," Opt. Express **29**, 19058–19067 (2021).
14. B. Hinkov, F. Pilat, L. Lux, P. L. Souza, M. David, A. Schwaighofer, D. Ristanić, B. Schwarz, H. Detz, A. M. Andrews, B. Lendl, and G. Strasser, "A mid-infrared lab-on-a-chip for dynamic reaction monitoring," Nat. Commun. **13**, 4753 (2022).
15. M. Sieger and B. Mizaikoff, "Toward on-chip mid-infrared sensors," Anal. Chem. **88**, 5562–5573 (2016).
16. U. Willer, M. Saraji, A. Khorsandi, P. Geiser, and W. Schade, "Near- and mid-infrared laser monitoring of industrial processes, environment and security applications," Opt. Laser Eng. **44**, 699–710 (2006).
17. C. Daffara, S. Parisotto, P. I. Mariotti, and D. Ambrosini, "Dual mode imaging in mid infrared with thermal signal reconstruction for innovative diagnostics of the 'Monocromo' by Leonardo da Vinci," Sci. Rep. **11**, 22482 (2021).
18. P. Werle, R. Mücke, and F. Slemr, "The limits of signal averaging in atmospheric trace-gas monitoring by tunable diode-laser absorption spectroscopy (TDLAS)," Appl. Phys. B **57**, 131–139 (1993).
19. A. Dabrowska, A. Schwaighofer, S. Lindner, and B. Lendl, "Mid-IR refractive index sensor for detecting proteins employing an external cavity quantum cascade laser-based Mach-Zehnder interferometer," Opt. Express **28**, 36632–36642 (2020).
20. H. Lin, Z. Luo, T. Gu, L. C. Kimerling, K. Wada, A. Agarwal, and J. Hu, "Mid-infrared integrated photonics on silicon: a perspective," Nanophotonics **7**, 393–420 (2017).
21. A. Malik, M. Muneeb, S. Pathak, Y. Shimura, J. Van Campenhout, R. Loo, and G. Roelkens, "Germanium-on-silicon mid-infrared arrayed waveguide grating multiplexers," IEEE Photon. Technol. Lett. **25**, 1805–1808 (2013).
22. Q. Liu, J. M. Ramirez, V. Vakarin, J. Frigerio, A. Ballabio, L. Vivien, C. Alonso-Ramos, G. Isella, and D. Marris-Morini, "Mid-IR integrated cavity based on Ge-rich graded SiGe waveguides with lateral Bragg grating," in *Mid-Infrared Coherent Sources 2018* (2018), paper MM3C.4.
23. L. Zhang, A. M. Agarwal, L. C. Kimerling, and J. Michel, "Nonlinear Group IV photonics based on silicon and germanium: from near-infrared to mid-infrared," Nanophotonics **3**, 247–268 (2014).
24. Z. Zhao, C.-M. Lim, C. Ho, K. Sumita, Y. Miyatake, K. Toprasertpong, S. Takagi, and M. Takenaka, "Low-loss Ge waveguide at the 2-μm band on an N-type Ge-on-insulator wafer," Opt. Mater. Express **11**, 4097–4106 (2021).
25. K. Gallacher, R. W. Millar, U. Griškevičiūte, L. Baldassarre, M. Sorel, M. Ortolani, and D. J. Paul, "Low loss Ge-on-Si waveguides operating in the 8–14 μm atmospheric transmission window," Opt. Express **26**, 25667–25675 (2018).
26. W. Li, P. Anantha, S. Bao, K. H. Lee, X. Guo, T. Hu, L. Zhang, H. Wang, R. Soref, and C. S. Tan, "Germanium-on-silicon nitride waveguides for mid-infrared integrated photonics," Appl. Phys. Lett. **109**, 241101 (2016).
27. A. Osman, M. Nedeljkovic, J. Soler Penades, Y. Wu, Z. Qu, A. Z. Khokhar, K. Debnath, and G. Z. Mashanovich, "Suspended low-loss germanium waveguides for the longwave infrared," Opt. Lett. **43**, 5997–6000 (2018).
28. D. Ren, C. Dong, S. J. Addamane, and D. Burghoff, "High-quality microresonators in the longwave infrared based on native germanium," Nat. Commun. **13**, 5727 (2022).
29. J. Lim, J. Shim, I. Kim, S. K. Kim, H. Lim, S.-Y. Ahn, J. Park, D.-M. Geum, and S. H. Kim, "Low-loss and high-confinement photonic platform based on germanium-on-insulator at mid-infrared range for optical sensing," J. Lightwave Technol. **41**, 2824–2833 (2023).
30. S. H. Kim, J.-H. Han, J.-P. Shim, H.-J. Kim, and W. J. Choi, "Verification of Ge-on-insulator structure for a mid-infrared photonics platform," Opt. Mater. Express **8**, 440–451 (2018).
31. S. H. Kim, D.-M. Geum, M.-S. Park, and W. J. Choi, "$In_{0.53}Ga_{0.47}As$-on-insulator metal–oxide–semiconductor field-effect transistors utilizing Y_2O_3 buried oxide," IEEE Electron Device Lett. **36**, 451–453 (2015).
32. A. Li, T. Van Vaerenbergh, P. De Heyn, P. Bienstman, and W. Bogaerts, "Backscattering in silicon microring resonators: a quantitative analysis," Laser Photon. Rev. **10**, 420–431 (2016).
33. P. E. Barclay, K. Srinivasan, and O. Painter, "Nonlinear response of silicon photonic crystal microresonators excited via an integrated waveguide and fiber taper," Opt. Express **13**, 801–820 (2005).
34. X. Jiang, H. Wu, and D. Dai, "Low-loss and low-crosstalk multimode waveguide bend on silicon," Opt. Express **26**, 17680–17689 (2018).

35. G. Moille, Q. Li, T. C. Briles, S.-P. Yu, T. Drake, X. Lu, A. Rao, D. Westly, S. B. Papp, and K. Srinivasan, "Broadband resonator-waveguide coupling for efficient extraction of octave-spanning microcombs," Opt. Lett. **44**, 4737–4740 (2019).
36. H.-T. Kim and M. Yu, "Cascaded ring resonator-based temperature sensor with simultaneously enhanced sensitivity and range," Opt. Express **24**, 9501–9510 (2016).
37. T.-H. Xiao, Z. Zhao, W. Zhou, C.-Y. Chang, S. Y. Set, M. Takenaka, H. K. Tsang, Z. Cheng, and K. Goda, "Mid-infrared high-*Q* germanium microring resonator," Opt. Lett. **43**, 2885–2888 (2018).
38. B. Troia, J. S. Penades, A. Z. Khokhar, M. Nedeljkovic, C. Alonso-Ramos, V. M. Passaro, and G. Z. Mashanovich, "Germanium-on-silicon Vernier-effect photonic microcavities for the mid-infrared," Opt. Lett. **41**, 610–613 (2016).
39. R. Morgan, C. Heidelberger, D. Kharas, K. Cahoy, and C. Sorace-Agaskar, "Low-loss germanium-on-silicon waveguides and ring resonators for the mid-wave infrared," in *Conference on Lasers and Electro-Optics*, *Technical Digest Series* (Optica Publishing Group, 2022), paper SW5O.1.
40. S. Radosavljevic, N. T. Beneitez, A. Katumba, M. Muneeb, M. Vanslembrouck, B. Kuyken, and G. Roelkens, "Mid-infrared Vernier racetrack resonator tunable filter implemented on a germanium on SOI waveguide platform [invited]," Opt. Mater. Express **8**, 824–835 (2018).
41. D. A. Kozak, N. F. Tyndall, M. W. Pruessner, W. S. Rabinovich, and T. H. Stievater, "Germanium-on-silicon waveguides for long-wave integrated photonics: ring resonance and thermo-optics," Opt. Express **29**, 15443–15451 (2021).
42. R. Armand, M. Perestjuk, A. D. Torre, M. Sinobad, A. Mitchell, A. Boes, J.-M. Hartmann, J.-M. Fedeli, V. Reboud, P. Brianceau, A. D. Rossi, S. Combrié, C. Monat, and C. Grillet, "Mid-infrared integrated silicon–germanium ring resonator with high *Q*-factor," APL Photon. **8**, 071301 (2023).
43. J. M. Ramirez, Q. Liu, V. Vakarin, X. Le Roux, J. Frigerio, A. Ballabio, C. Alonso-Ramos, E. T. Simola, L. Vivien, G. Isella, and D. Marris-Morini, "Broadband integrated racetrack ring resonators for long-wave infrared photonics," Opt. Lett. **44**, 407–410 (2019).
44. K. Zhang, G. Böhm, and M. A. Belkin, "Mid-infrared microring resonators and optical waveguides on an InP platform," Appl. Phys. Lett. **120**, 061106 (2022).
45. J. Haas, P. Artmann, and B. Mizaikoff, "Mid-infrared GaAs/AlGaAs micro-ring resonators characterized via thermal tuning," RSC Adv. **9**, 8594–8599 (2019).
46. P. Ma, D.-Y. Choi, Y. Yu, Z. Yang, K. Vu, T. Nguyen, A. Mitchell, B. Luther-Davies, and S. Madden, "High *Q* factor chalcogenide ring resonators for cavity-enhanced MIR spectroscopic sensing," Opt. Express **23**, 19969–19979 (2015).
47. Y. Chen, H. Lin, J. Hu, and M. Li, "Heterogeneously integrated silicon photonics for the mid-infrared and spectroscopic sensing," ACS Nano **8**, 6955–6961 (2014).